Stability of Argyrodite Electrolyte in Li-In Based All-Solid-State Batteries

*Di Huang, Gao Liu, Wei Tong**

Energy Storage and Distributed Resources Division, Lawrence Berkeley National Laboratory, Berkeley, California 94720, United States

Email: weitong@lbl.gov

ABSTRACT

Li-In alloy has been largely used as a working anode in all solid-state full cells. Incorporating indium can help stabilize the interface by suppressing the decomposition of the solid electrolyte. However, the Li-In phase diagram is complex and involves multiple phases, depending on the composition. Understanding the relationship between the Li-In composition and electrochemical performance, as well as identifying the root causes of cell failure, is crucial for advancing this technology. Here, we present a compressive analysis of the impact of the Li-In composition on the interfacial stability of the argyrodite electrolyte in all solid-state batteries. We find that the $Li_{0.5}In$ alloy, composed of LiIn and In phases, significantly improves the interfacial stability. In contrast, when using Li-In or Li metal anode, we observe the accumulation of large Li deposits within the solid electrolyte as well as a thick interface composed of Li_2S, leading to the shortened cycle life. $Li_{0.5}In$ anode enables a high critical current density of 2.0 mA cm^{-2} and extends cycling for 1000 h at 0.5 mA cm^{-2}. Additionally, a reversible capacity of 120 mAh g^{-1} is achieved over 700 cycles in the $LiCoO_2|Li_6PS_5Cl|$ $Li_{0.5}In$ full cell.

KEYWORDS: all solid-state batteries, full cells, symmetric cells, interfacial stability, Li_6PS_5Cl argyrodite electrolyte, Li-In alloy, Li deposit

INTRODUCTION

Lithium-ion batteries (LIBs) are the primary power sources for a wide range of devices, spanning from the portable electronics to electric vehicles (EVs). Despite their success in the portable electronics, further advancements in LIB technology are essential to facilitate the wide adoption of EVs. Conventional LIBs that rely on the organic liquid electrolytes and graphite anode have persistently encountered the challenges in driving range and safety. All solid-state batteries that eliminate the flammable liquid electrolytes could potentially address the safety concern.[1-3] Furthermore, all solid-state batteries hold a great potential to enable the use of Li metal anode, surpassing the capacity limitation of graphite anode. However, it remains a challenge to find a suitable solid electrolyte (SE) that meets all the requirements to replace the liquid electrolytes. While considerable progress has been made in identifying solid electrolytes with high ionic conductivity and stability, practical viability is hindered by the issues such as the inferior chemical/electrochemical stability, poor physical interface contact, and air sensitivity.

The commonly studied solid electrolytes include oxides, sulfides, halides, polymers, and hybrid materials. Among them, lithium argyrodite, Li_6PS_5Cl (LPSC), has drawn significant attention because of its high ionic conductivity (>1 mS cm^{-1}) and good mechanical properties. Moreover,

argyrodite electrolyte tends to enabling better cycling with Li and Li-In anode compared to sulfide and halide electrolyte systems, and has been used as an additional layer between sulfide/halide electrolytes and Li or Li-In anodes in all solid-state cells.[4-6] The first argyrodite structure was discovered in the mineral Ag_8GeS_6, which is an excellent Ag ion conductor.[7, 8] Later, it was found that the Ag ions in the argyrodite structure can be substituted by other cations, such as Cu^+, which led to the development of a new series of Cu-argyrodite conductors. Given the fact that the radii of Cu^+ and Li^+ are similar (Cu^+=74 pm, Li^+=73 pm), an attempt to substitute Cu^+ by Li^+ was made to fabricate a Li^+ conductor. In 2008, Deiseroth *et al.* reported the discovery of Li_6PS_5X (X=Cl, Br, I), a new class of argyrodite materials, which exhibited a high Li^+ conductivity, making them as a promising candidate for solid electrolyte.[9] However, further enhancements in the stability of Li_6PS_5X are indispensable for its practical implementation. Because of the low electrochemical potential (-3.04 V *vs.* RHE) of Li metal, Li-argyrodite is thermodynamically unstable in contact with Li and is reduced to Li_2S, P_2S_5, LiCl *et al.*[10] There hasn't been a clear path to address the interfacial stabilities with Li metal anode due to the nature of the high reactivity.[11, 12] Designing and engineering the argyrodite/Li metal interface with augmented chemical and electrochemical stability, optimal physical contact, and superior ionic conductivity is of paramount importance. As an alternative, Li metal alloy (e.g., Li-In, Li-Au) has been used in all solid-state batteries due to their lower reducing potential and improved interfacial stability, particularly when tackling the issues beyond the anode.[13-19] Nonetheless, there has been limited research devoted to understanding the interfacial stability of the argyrodite electrolyte with Li-In anode. Particularly, Li-In alloy system involves multiple phases, depending on the composition. The composition of Li-In anode varies during charge and discharge processes, which leads to different electrochemical properties and thus distinct behaviors upon contact with argyrodite electrolyte.[20]

In this study, our primary goal is to examine the impact of the Li-In alloy composition, focusing particularly on the interfacial reactions between the LPSC argyrodite and anodes. We conduct comprehensive electrochemical analysis on the symmetric cells with Li, LiIn, and $Li_{0.5}In$ anodes using galvanostatic cycling, electrochemical impedance spectroscopy (EIS), and cyclic voltammetry (CV). Remarkably, the $Li_{0.5}In|Li_6PS_5Cl|Li_{0.5}In$ symmetric cell exhibits a high critical current density (CCD) of 2 mA cm^{-2} and maintains stable cycling for over 1000 h at 0.5 mA cm^{-2} with no sign of soft short. Subsequent post-mortem analysis is conducted on the cycled cells using a combination of scanning electron microscopy (SEM), energy-dispersive X-ray spectroscopy (EDS), and X-ray photoelectron spectroscopy (XPS). Our findings highlight the pivotal role of indium in facilitating the interfacial stability of argyrodite electrolyte, thereby enabling the long-term cycling. $Li_{0.5}In$ anode effectively suppresses the decomposition of argyrodite electrolyte and dead Li deposition within the SE due to its elevated redox potential. Additionally, we observe the larger Li metal deposits (1 – 5 μm) within the SE layer, accompanied by the formation of Li_2S at the interfaces with LiIn and Li anodes. Using $Li_{0.5}In$ anode, a full cell incorporating $LiNbO_3$ coated $LiCoO_2$ demonstrates stable cycling for 700 cycles at a reversible capacity of 120 mAh g^{-1}. Overall, our study reveals the interfacial stability of the LPSC electrolyte with different Li-in anodes and underscores the importance of scrupulous anode composition for accurate electrochemical assessments of other components in all solid-state cells.

EXPERIMENTAL SECTION

Material Synthesis

LPSC powder was prepared by a solid-state reaction. Commercially available Li_2S, P_2S_5, and LiCl precursors were weighed at the stoichiometric ratio and then loaded into a zirconia jar inside an Ar-filled glove box. The mixed powders were milled at 550 rpm for 24 h and sealed inside a quartz tube for calcination at 550 °C for 5 h under Ar flow. $LiNbO_3$ coated $LiCoO_2$ was prepared by a sol-gel method using lithium ethoxide and niobium ethoxide (Li: Nb = 1: 1) as the precursors. $LiCoO_2$ powder was first dispersed in ethanol and then a designated amount of the Li and Nb precursors dissolved in ethanol (1.4 wt% $LiNbO_3$) was added. The mixture was stirred to achieved full mixing and then dried overnight. Afterwards, the mixture was annealed under O_2 at 450 °C for 1 h to obtain $LiNbO_3$ coated $LiCoO_2$.

Physical Characterization

XRD patterns were collected on the Bruker D2-Phaser with Cu Kα radiation (λ = 1.54178 Å) from 10 to 70 degree. The SEM and EDS images were collected on Zeiss Gemini Ultra-55 Analytical Field Emission Scanning Electron Microscope coupled with the Bruker X-Ray Energy Dispersive Spectrometer with the beam energy of 7 kV. The 200kV FEI monochromated F20 UT Tecnai was used to perform optimum high resolution TEM experiment. Soft X-ray absorption spectroscopy (XAS) was carried out on beamline 8-2 at the Stanford Synchrotron Radiation Laboratory and data were acquired under ultrahigh vacuum (10^{-9} Torr) in a single load at room temperature using total electron yield (TEY) via the drain current. X-ray photoelectron spectroscopy (XPS) experiment was conducted on a Thermo Fisher K-Alpha Plus XPS/UPS analyzer (operating pressure of 2.0×10^{-7} Pa) with a monochromatic Al X-ray source (1.486 eV) at The Molecular Foundry. Samples for XPS analysis were prepared inside an Ar-filled glovebox using an air-free sample holder with Ag-tape on the Si-substrate. LPSC pellets for the EIS measurements were prepared by loading 200 mg powder to the PEEK cells with a diameter of 12 mm and then pressed under various pressures. EIS spectra were collected using the stainless steel as the blocking electrodes in the frequent range of 1 MHz to 100 mHz with an amplitude voltage of 20 mV. The electrical conductivity was measured using the DC polarization method. The pellet was polarized from 0.3 to 0.7 V for 30 min. The resistance was calculated by the linear fitting between the polarized voltage and stabilized current.

Electrochemical Characterization

150 mg LPSC powder was loaded and cold pressed inside a PEEK cell (12 mm in diameter) under 400 MPa for 5 min. The Li-In alloy or pure Li was added onto both sides and pressed under 120 MPa for 5 min. The Li-In anodes were prepared by pressing Li and In foils together at the designated ratios under 120 MPa. Li-In anode is used as a general term to differentiate from the Li or In metal anode while LiIn and $Li_{0.5}In$ indicates the alloy composition. The cell was tested at room temperature with a stack pressure of 20 MPa. For CCD measurement, the current density increased from 0.1 mA cm^{-2} with a step size of 0.1 mA cm^{-2}, and each current density is tested for 1 cycle. For the symmetric cell cycling, the platting/stripping was conducted at a constant current for 1 h, respectively. The EIS measurements were conducted after stripping at selected current densities in the frequent range of 1 MHz to 100 mHz with an amplitude voltage of 20 mV. CV was performed after selected cycles within the voltage range of -0.08 to 0.08 V at a rate of 0.1 mV s^{-1}. The ionic conductivity is calculated using the equation $\sigma = \frac{I}{RA}$, where □ is the ionic conductivity, I is the thickness of the pellet, R is the bulk resistance measured by EIS, and A is the area of the pellet.

The cathode mixture was prepared by mixing 70 wt% of $LiNbO_3$ coated $LiCoO_2$ with 30 wt% Li_6PS_5Cl. The cell was prepared using a PEEK cell (12 mm in diameter). The SE layer was fabricated by pressing 75 mg of Li_6PS_5Cl under 200 MPa for 5min. ~11 mg of the cathode mixture was uniformly spread onto one side of the SE and pressed under 450 MPa for 5 min. The Li-In alloy was then added onto the other side of the SE and pressed under 120 MPa. Galvanostatic charge-discharge was performed within the voltage window of 3.0 and 4.3 V vs. Li/Li^+ at 0.1 C (1C = 140 mAh g^{-1}) under the stack pressure of 20 MPa. For the test of $LiCoO_2$ half-cell with liquid electrolyte, the slurry was prepared by mixing active $LiCoO_2$, polyvinylidene fluoride (PVDF), and carbon in N-methylpyrrolidone (NMP) solvent at a weight ratio of 80:10:10. The slurry was cast on the aluminum foil and dried inside the vacuum chamber at 120 °C overnight. 2032-type coin cell was assembled with Li metal anode, Celgard 2400 separator, and 1.2 M $LiPF_6$ in ethylene carbonate: ethylmethyl carbonate (EC: EMC) (3: 7 by weight) electrolyte. The Galvanostatic charge-discharge was performed within the voltage window of 3.0 and 4.3 V vs. Li/Li^+ at 0.1 C (1C = 140 mAh g^{-1}) using the Arbin battery testing station.

RESULTS AND DISCUSSION

LPSC argyrodite was prepared by a conventional solid-state reaction (**Figure 1A**). Precursors were mixed by a high-energy milling process and followed by a calcination process to increase the crystallinity and ionic conductivity of the final product.[21] XRD pattern (**Figure 1B**) reveals a typical cubic argyrodite structure with a space group $F\bar{4}3m$, consistent with the pattern reported in the literature.[22] The Bragg peak at ~52° and the broad one between 15 and 40° originate from the air-tight holder. Other than these peaks, there are no additional ones revealed by XRD, indicating the formation of pure LPSC phase with no crystalline impurities within the detection limit. The SEM image (**Figure 1B** inset) shows the irregular shape of LPSC particles with a size of a few micrometer, which is quite common for the solid-state reaction. The as-produced LPSC powder is compacted into the pellets and assembled with a customized solid-state cell (**Figure 1C**) for conductivity measurements. The stainless-steel rods on each side are current collectors, while they also provide a stack pressure to maintain the good interfacial contact. The ionic conductivity of the LPSC pellet is measured under different stack pressures (**Figure S1A**). Clearly, the measured ionic conductivity highly depends on the stack pressure applied during the measurement. The bulk resistance of the LPSC pellet decreases with increasing stack pressure, showing a higher ionic conductivity under a higher stack pressure due to the better contacts (e.g., current collector and LPSC pellet, among LPSC particles). In pursuit of the precise measurement of the ionic conductivity, we also explore the influence of the pressing pressure (**Figure 1D**) that is applied during the preparation of the LPSC pellet and directly affect the physical contact among LPSC particles. In principle, a higher pressing pressure leads to a denser pellet with less porosity. As shown in **Figure 1D**, the measured ionic conductivity increases from 1.41 to 2.14 mS cm^{-1} with increasing the pressing pressure from 200 to 400 MPa. Correspondingly, the pellet density increases from 84.8% to 92.2% relative to its theoretical density (1.64 g cm^{-3}). When further increasing the pressing pressure to 500 MPa, the pellet density goes up to 96.0%, while the measured ionic conductivity drops to 1.51 mS cm^{-1}. This is perhaps due to the cracks formed under the high pressing pressure.[23] As a result, the measured ionic conductivity is highly sensitive to the pressing and stack pressure. The optimal pressing and stack pressure are 400 and 130 MPa, respectively, for the pellet in this study (200 mg & 12 mm in diameter). We note that the optimal pressing and stacking pressure likely vary with the pellet dimension (thickness and diameter),

therefore, they should be optimized for the conductivity measurement for any given study.[17, 24-26] Accordingly, the direct current (DC) polarization method (**Figure 1E**) is used to measure the electrical conductivity of the LPSC pellet prepared with 400 MPa pressing pressure and 130 MPa stack pressure. The linear fitting of voltage and current is shown in **Figure S1B**. The electrical conductivity is calculated to be 5.6×10^{-9} S cm^{-1}. Overall, the fabrication of the as-produced LPSC argyrodite electrolyte has been optimized to exhibit optimal conductivities under the testing conditions.

To benchmark the interfacial stability of Li_6PS_5Cl against metallic Li, Li|Li_6PS_5Cl|Li symmetric cell is assembled inside an Ar-filled glove box. **Figure 2A** shows the critical current density (CCD) of the Li/ Li_6PS_5Cl /Li cell from 0.1 to 0.4 mA cm^{-2}. A slight voltage drop at 0.3 mA cm^{-2} indicates a potential soft short circuit. EIS spectra (**Figure 2B**) are collected after stripping at each current density test to assess the failure mechanism. The high-frequency intercept in the EIS spectra corresponds to the bulk resistance of the symmetric cell, while the semicircle in the low-frequency region indicates the interfacial resistance, stemming from the SEI and charge transfer resistance.[27] EIS collected after 0.1 mA cm^{-2} remains almost identical to the pristine state, while the bulk resistance slightly decreases after 0.2 mA cm^{-2}. In comparison, a significant decrease in bulk resistance to 28 Ω is observed after 0.3 mA cm^{-2} and 15 Ω after 0.4 mA cm^{-2}, suggesting the soft short circuits occurs after 0.3 mA cm^{-2}. Furthermore, a semicircle in the low-frequency region is attributed to the formation of the solid electrolyte interface (SEI). Additionally, CV is performed to gain deeper insights into the failure mechanism, which effectively signifies the soft short circuit in all solid-state cells.[28] Similarly, the CV profiles (**Figure 2C**) after 0.1 and 0.2 mA cm^{-2} are nearly identical to that obtained at the pristine state. However, after 0.3 and 0.4 mA cm^{-2}, there is a substantial increase in peak current, confirming the onset of a soft short circuit. The Li symmetric cell test reveals the CCD of 0.2 mA cm^{-2} and soft short circuit at a higher current density. Different from an immediate voltage drops to 0 V for hard-short circuit, when soft-short takes place, lithium filaments grow from one electrode to the other, but the growth is smaller than that in a hard-short circuit. In this scenario, both electron and ion flows occur at the same time, while some electrons stay inside the cell, others may flow to an external circuit. The measured current results from combined electron and ion flows; therefore, soft-short circuit is a dynamic process and the cell voltage behavior could vary.[29] This process is also regarded as the "fake stable" phenomenon, rather than interfacial stabilization process.[30, 31] The long-term cycling of Li|Li_6PS_5Cl|Li symmetric cell at 0.1 mA cm^{-2} is shown in **Figure 2D**. The corresponding EIS and CV data after certain cycles are presented in **Figure S2**. Overall, the polarization voltage slightly increases upon cycling. Meanwhile, the bulk resistance observed from the EIS measurements increases and the peak current in the CV profiles gradually decreases. These observations suggest that the increased polarization voltage during cycling stems from the decreased ionic conductivity, primarily induced by the interfacial reaction of the solid electrolyte (formation of SEI). The SEI layer could contain the degradation products such as Li_2S, Li_3PS_4, and LiCl, which exhibit lower ionic conductivity.[10] After about 240 h platting/stripping, a distinct voltage drop marks the onset of hard short circuit. This is also verified by the EIS and CV tests (**Figure S2**). From the EIS, the bulk resistance after short circuit reduces to nearly zero. Meanwhile, the CV curve turns into a nearly vertical line, implying the entire cell turns into a good electrical conductor. The argyrodite electrolyte is electrochemically unstable against Li metal. Even under low current densities, the gradual interfacial degradation persists, eventually leading to soft and hard short circuits.

The Li-In alloy is often used as an alternative anode in all solid-state cells due to its high reduction potential. To understand the effect of the Li-In composition on the cell performance, two Li-In with different compositions, namely, LiIn alloy and $Li_{0.5}In$ alloy consisting of In and LiIn phases, are prepared to assemble the $Li_{0.5}In|Li_6PS_5Cl|Li_{0.5}In$ (**Figure 3**) and $LiIn|Li_6PS_5Cl|LiIn$ (**Figure S4**) symmetric cells. For the CCD test of $Li_{0.5}In|Li_6PS_5Cl|Li_{0.5}In$ cell, there is no noticeable soft or hard short circuit at a current density up to 2.5 mA cm^{-2} (**Figure 3A**). Compared to the CCD of the $Li|Li_6PS_5Cl|Li$ symmetric cell (0.2 mA cm^{-2}), the argyrodite electrolyte is apparently more stable with Li-In alloy. As expected, an increased overpotential with increasing current density is observed during the platting/stripping processes, and becomes more significant at high current densities above 2.0 mA cm^{-2}. [32-34] The EIS spectra (**Figure 3B**) collected after stripping at each current density test show that the bulk resistance remains almost constant below 2 mA cm^{-2}. In contrast, the interfacial resistance (the diameter of the semicircle) enlarges with increasing current density. The EIS results suggest that a high current induces more pronounced LPSC decomposition and SEI formation, consequently an elevated interfacial resistance.[35] This is consistent with the gradual voltage increase during each plating/stripping process. However, when the current surpasses 2 mA cm^{-2}, the bulk resistance exhibits a rapid surge, which is consistent with the substantial overpotential observed above 2 mA cm^{-2} during the plating/striping processes. Meanwhile, the peak current exhibits a sudden drop above 2 mA cm^{-2} during the CV scan (**Figure 3C**). The combined electrochemical characterization suggests that above the CCD of 2.0 mA cm^{-2}, the degradation of the solid electrolyte becomes severe and deteriorates the cell performance. Additionally, at the high current densities, the voltammogram during the CV scan begins to exhibit a behavior akin to the double layer capacitance observed at the interface between a surface and fluid. Ideally, the CV curve of the solid electrolyte resembles a straight line, as seen in the voltammogram of the pristine state, owing to its high ionic conductivity. When the degradation occurs, the ionic conductivity diminishes, and the solid electrolyte starts to behave like a capacitor. Correspondingly, the voltammogram exhibits the characteristic 'duck shape' (2.1 mA cm^{-2}). To gain deeper insights into the long-term stability, the symmetric cells are cycled at 0.5 and 1.0 mA cm^{-2}. They both show stable voltage profiles for over 1000 h, indicating $Li_{0.5}In$ alloy improves the stability of LPSC electrolyte. However, noticeable drops in overpotential occurs during cycling around 80 h and 600 h at 1 mA cm^{-2}. From the EIS spectra (**Figure S3B**) collected during cycling, there is no obvious change in bulk resistance, but the interfacial resistance increases significantly after 40 cycles (~80 h). Moreover, comparison of the impedance at 0.5 and 1 mA cm^{-2} (**Figure S3A, B**) shows that the interfacial resistance is greater at elevated current density, implying severe interfacial reactions.[35] With the LiIn alloy anode, the symmetric cell cycles at 0.5 mA cm^{-2} for about 1000 h (**Figure S4A**). The overpotential during cycling appears unstable and significantly higher than that of $Li_{0.5}In$ (~0.3 V vs. ~0.03 V, nearly 10 times higher), implying the severe interfacial reaction.[20, 28, 36] This is also evidenced by the significantly higher interfacial resistance (R_{SEI+CT}) for the LiIn cell compared to the $Li_{0.5}In$ one during the early cycles, while the LiIn cell eventually becomes soft shorted (**Figure S4B, C**).

The symmetric cells after cycling are then disassembled for post-mortem analysis to understand the impact of the Li-In alloy composition on the SEI evolution. The top-view and cross-section SEM images of pristine SE pellet are shown in **FigureS5**. In comparison, the SEM images (**Figure 4**) reveal the pronounced changes in the morphology of the SE after cycling. **Figure 4A, B** show the top view of the LPSC solid electrolyte cycled with $Li_{0.5}In$ and LiIn anode, respectively. They both

exhibit similar morphology, with most areas covered by the Li filaments. **Figure 4C-E** show the SEM images and corresponding cross-section EDS maps of the $Li_{0.5}In|Li_6PS_5Cl$, $LiIn|Li_6PS_5Cl$, and $Li|Li_6PS_5Cl$ interfaces, respectively. For the sake of clarify, only color maps of the element S, P, and O are shown. The distribution of S, P mostly represents the distribution of the LPSC electrolyte, while O shows the presence of Li originating from the oxidized Li during sample transfer. Clearly, the anode composition leads to a significant difference regarding the distribution of Li after extensive cycling. With $Li_{0.5}In$ anode, only sparse Li scatters within the SE layer. In comparison, an increased amount of Li metal with a larger size (up to ~1 μm) is revealed inside the SE when the LiIn anode is used. A similar phenomenon but an even larger size of Li (up to ~5 μm) is observed inside the SE with pure Li anode. The SEM and EDS results suggest that the anode composition has a significant impact on the formation and growth of Li filaments, and the dead Li still forms with the use of Li-In anode. However, the presence of excess In largely confines the Li inside the anode layer, slows down the dead Li formation, and thus extends the cycle life.

X-ray photoemission spectroscopy (XPS) is also employed to examine the chemical compositions of the interfaces (**Figure 5**). The XPS spectra of Cl for the interfaces with both Li-In anodes are dominated by the peaks attributed to the Cl 2p in the LPSC electrolyte (**Figure S6**). In the XPS spectra of P 2p, besides the characteristic peaks of the argyrodite, an additional peak at a binding energy of 131.3 eV is revealed on the interfaces of both anodes, indicating the SEI component with reduced P. Moreover, the XPS spectra of S 2p consist of the doublet feature, with S $2p_{3/2}$ at a binding energy of 162.5 and 161.3 eV, which is ascribed to the S in LSPC electrolyte. Notably, a distinct peak at 160.1 eV that is attributed to Li_2S is observed on the LiIn surface, in sharp comparison, no such a Li_2S peak is detected on the $Li_{0.5}In$ surface. These results suggest that the excess Li in LiIn alloy facilitates the decomposition of LPSC electrolyte and preferentially forms Li_2S. Furthermore, we note that the features of In $3d_{5/2}$ doublet In 3d spectra can be clearly detected on the interface of $Li_{0.5}In$ anode (**Figure S6**). In contrast, the In 3d signals are not readily collected on the interface of LiIn anode after examining over 10 samples. Considering the probing depth limit of XPS, we infer that the severe interfacial reaction at the LiIn interface leads to the formation of a thick and dense SEI, which blocks the signal from the In in the LiIn anode. This further aligns with the high overpotential observed for the LiIn|LPSC|LiIn cell. The thick SEI at the interface of LiIn and SE with sluggish Li diffusion impedes the Li^+ transport. The XPS analysis suggests that the $Li_{0.5}In$ alloy is more stable towards LPSC electrolyte, while the Li-In alloy facilitates the formation of Li_2S that is an inferior SEI component. The distinguished behaviors of the Li-In alloys are likely due to the different potentials of the Li-In alloy compositions. $Li_{0.5}In$ exhibits a high equilibrium redox potential (~ 0.6 V vs. Li^+/Li), while LiIn exhibits a low equilibrium redox potential close to pure Li.[20] Similar to the case with pure Li, LPSC is readily reduced at the low potential and facilitates the Li dendrite formation.

We then assemble the full cells using 1.4 wt% $LiNbO_3$ coated $LiCoO_2$ (LNO-LCO) as cathode material, LPSC as SE, and LiIn and $Li_{0.5}In$ alloys as anodes. LNO-LCO cathode is prepared by a sol-gel method.[37] LNO coating provides protection for LCO cathode and eliminates the effect of the space charge at the cathode interface.[38-40] **Figure 6A** shows the XRD pattern of LCO cathode before and after LNO coating, revealing no change in the crystal structure. Coated LCO remains the well-ordered layered structure with no detectable crystalline phase within the detection limit. The high-resolution transmission electron microscopy (TEM) analysis reveals a uniform coating

with a thickness of ~5 nm on the LCO surface (**Figure 6B**). The impact of LNO coating on the electrochemical performance of the LCO cathode is evaluated in the cells with a liquid electrolyte (**Figure S7**). They both exhibit a similar initial capacity of >150 mAh g^{-1} with almost identical charge/discharge profiles and plateaus around 3.9, 4.08, and 4.18 V.[41, 42] A slight capacity drop for the coated LCO is likely due to the Li loss during coating process, while the capacity of the coated LCO remains stable around 140 mAh g^{-1} after 150 cycles. Therefore, the coating process shows a minimal impact on the structure and electrochemistry of the LCO cathode. We then assemble the solid-state full cells with different anodes. Among all the tested anodes, $Li_{0.5}In$ anode enables the best performance with a high initial capacity of 125 mAh g^{-1} and 120 mAh g^{-1} being maintained after 700 cycles (**Figure 6C**). **Figure S8A** shows the soft XAS spectra of Co *L*-edge of coated LCO at pristine and 500th discharged states. They both show typical peaks at ~781 and ~795 eV with no evidence of energy change after cycling, consistent with previous report.[43] The soft XAS results further confirm the sufficient protection of LCO surface by LNO coating. An initial capacity drop occurs during the first 10 cycles, consistent with the higher polarization on the voltage profiles (**Figure 6D**), which could due to the SEI formation. After 50 cycles, the capacity gradually increases and stabilizes around 200 cycles. Correspondingly, the voltage profiles also shift back with a lower polarization. One possible explanation is that the variation in the Li content of the LCO cathode affects the electrode conductivity because the conductivity of the delithiated LCO varies with the Li content. We make a close comparison of the voltage profiles of the full cell using $Li_{0.5}In$, LiIn, and In anodes (**Figure S8B, C**). The all solid-state cell with pure Li anode is shorted quickly, suggesting the severe interfacial reaction. While the cell with pure In anode exhibits similar charge profiles, but a low discharge capacity of 91 mAh h^{-1}, which could be due to the poor physical contact. In comparison, the cell with LiIn anode exhibits a higher capacity (125 mAh h^{-1}) but a higher polarization, likely due to the interfacial reaction between the LPSC electrolyte and excess Li. Overall, the composition of the Li-In anode is crucial to the all solid-state full cell performance while the challenges associated with the cathode could be temporarily addressed. The optimal Li content is necessary, so that the Li-In anode composition remains in the In/LiIn phase range during cycling. Furthermore, the Li content in the Li-In anode needs to be tuned to compensate the Li loss caused by the interfacial reaction and enhance the columbic efficiency.

CONCLUSIONS

In this work, we show that the measured conductivity of Li_6PS_5Cl electrolyte is influenced by the pressing and stack pressure, requiring careful optimization for specific experimental conditions. Additionally, we investigate the effect of the Li-In anode composition on the interfacial stability of the argyrodite electrolyte and electrochemical performance. Compared to the low CCD of 0.2 mA cm^{-2} observed with a pure Li anode, a symmetric cell using $Li_{0.5}In$ anode exhibits a significantly higher CCD of 2.0 mA cm^{-2} and maintains stable cycling for 1000 h at 0.5 mA cm^{-2}. The interfacial stability is highly dependent on the Li-In alloy composition, favoring the higher redox potentials for Li deposition. LiIn alloy is insufficient to prevent the interfacial reactions, leading to pronounced SE decomposition and formation of Li_2S at the interfaces. It also results in the accumulation of large Li deposits within the SE in the cells with excess Li. Stable cycling at a capacity of 120 mAh g^{-1} for 700 times is achieved in $LiCoO_2|Li_6PS_5Cl|Li_{0.5}In$ full cell. The key to achieving the stable full-cell cycling lies in mitigating the Li deposition within the SE during cycling, which helps suppress the interfacial reaction and provides sufficient Li inventory for high capacity and columbic efficiency. These findings provide useful guidance for designing the full-cell

configuration, especially regarding the Li-In composition. It's crucial to consider the true Li-In composition during full charge and discharge to mitigate the severe interfacial side reactions as well as enough Li inventory.

ASSOCIATED CONTENT

Supporting Information. EIS under different stack pressures and linear fit of voltage and current measured by DC polarization. EIS, CV, and voltage profiles of symmetric cells. SEM images of the pristine SE pellet. XPS of Cl 2p and In 3d on Li_6PS_5Cl interfaces. Soft XAS Co *L*-edge spectra of cycled LCO. Electrochemical performance of LCO full cells.

AUTHOR INFORMATION

Corresponding Author

Wei Tong - Energy Storage and Distributed Resources Division, Lawrence Berkeley National Laboratory, Berkeley, California 94720, United States; orcid.org/0000-0001-8328-7999; Email: weitong@lbl.gov

Authors

Di Huang - Energy Storage and Distributed Resources Division, Lawrence Berkeley National Laboratory, Berkeley, California 94720, United States; orcid.org/0000-0003-3698-5158; Email: dhuang@lbl.gov

Gao Liu - Energy Storage and Distributed Resources Division, Lawrence Berkeley National Laboratory, Berkeley, California 94720, United States; orcid.org/0000-0002-9263-5614; Email: gliu@lbl.gov

Notes

The authors declare no competing financial interest.

ACKNOWLEDGMENTS

This work is supported by the Assistant Secretary for Energy Efficiency and Renewable Energy, Office of Vehicle Technologies of the U.S. Department of Energy under Contract No. DE-AC02-05CH11231. Use of resources at the Molecular Foundry is supported by the Office of Science, Office of Basic Energy Sciences, of the U.S. Department of Energy under Contract No. DE-AC02-05CH11231. Use of the Stanford Synchrotron Radiation Lightsource, SLAC National Accelerator Laboratory, is supported by the U.S. Department of Energy, Office of Science, Office of Basic Energy Sciences under Contract No. DE-AC02-76SF00515. The authors appreciate the technical supports provided by Dr. Tevye R. Kuykendall at the Inorganic Nanostructures and Dr. Virginia Altoe at the Imaging and Manipulation of Nanostructures, Molecular Foundry.

REFERENCE

1. Wang, C.; Adair, K.; Sun, X., All-Solid-State Lithium Metal Batteries with Sulfide Electrolytes: Understanding Interfacial Ion and Electron Transport. *Acc. Mater. Res.* **2022**, 3, 1, 21–32.
2. Lim, H.-D.; Park, J.-H.; Shin, H.-J.; Jeong, J.; Kim, J. T.; Nam, K.-W.; Jung, H.-G.; Chung, K. Y., A Review of Challenges and Issues Concerning Interfaces for All-Solid-State Batteries. *Energy Storage Mater.* **2020,** *25*, 224-250.
3. Yu, C.; Zhao, F.; Luo, J.; Zhang, L.; Sun, X., Recent Development of Lithium Argyrodite Solid-State Electrolytes for Solid-State Batteries: Synthesis, Structure, Stability and Dynamics. *Nano Energy* **2021,** *83,* 105858.
4. Wang, C.; Liang, J.; Luo, J.; Liu, J.; Li, X.; Zhao, F.; Li, R.; Huang, H.; Zhao, S.; Zhang, L.; Wang, J.; Sun, X., A Universal Wet-Chemistry Synthesis of Solid-State Halide Electrolytes for All-Solid-State Lithium-Metal Batteries. *Sci. Adv.* **2021,** *7* (37), eabh1896.
5. Koç, T.; Hallot, M.; Quemin, E.; Hennequart, B.; Dugas, R.; Abakumov, A. M.; Lethien, C.; Tarascon, J.-M., Toward Optimization of the Chemical/Electrochemical Compatibility of Halide Solid Electrolytes in All-Solid-State Batteries. *ACS Energy Lett.* **2022,** *7* (9), 2979-2987.
6. Zhou, L.; Zuo, T.-T.; Kwok, C. Y.; Kim, S. Y.; Assoud, A.; Zhang, Q.; Janek, J.; Nazar, L. F., High Areal Capacity, Long Cycle Life 4 V Ceramic All-Solid-State Li-Ion Batteries Enabled by Chloride Solid Electrolytes. *Nat. Energy* **2022,** *7* (1), 83-93.
7. Winkler, C., Germanium, Ge, ein neues, nichtmetallisches Element. *Ber. Dtsch. Chem. Ges.* **1886,** *19*, 210-211.
8. Weisbach, A., Argyrodit, ein neues Silbererz. Neues Jahrbuch für Mineralogie, Geologie und Paläontologie. **1886**, 2, 67-71.
9. Deiseroth, H. J.; Kong, S. T.; Eckert, H.; Vannahme, J.; Reiner, C.; Zaiß, T.; Schlosser, M., Li_6PS_5X: A Class of Crystalline Li-Rich Solids With an Unusually High Li^+ Mobility. *Angew. Chem.* **2008,** *120*, 767-770.
10. Tan, D. H.; Wu, E. A.; Nguyen, H.; Chen, Z.; Marple, M. A.; Doux, J.-M.; Wang, X.; Yang, H.; Banerjee, A.; Meng, Y. S., Elucidating Reversible Electrochemical Redox of Li_6PS_5Cl Solid Electrolyte. *ACS Energy Lett.* **2019,** *4* (10), 2418-2427.
11. Tan, D. H.; Chen, Y.-T.; Yang, H.; Bao, W.; Sreenarayanan, B.; Doux, J.-M.; Li, W.; Lu, B.; Ham, S.-Y.; Sayahpour, B., Carbon-Free High-Loading Silicon Anodes Enabled by Sulfide Solid Electrolytes. *Science* **2021,** *373* (6562), 1494-1499.
12. Lee, Y.-G.; Fujiki, S.; Jung, C.; Suzuki, N.; Yashiro, N.; Omoda, R.; Ko, D.-S.; Shiratsuchi, T.; Sugimoto, T.; Ryu, S., High-Energy Long-Cycling All-Solid-State Lithium Metal Batteries Enabled by Silver–Carbon Composite Anodes. *Nat. Energy* **2020,** *5* (4), 299-308.
13. Kato, A.; Kowada, H.; Deguchi, M.; Hotehama, C.; Hayashi, A.; Tatsumisago, M., XPS and SEM Analysis Between Li/Li_3PS_4 Interface with Au Thin Film for All-Solid-State Lithium Batteries. *Solid State Ion.* **2018,** *322*, 1-4.
14. Nagao, M.; Hayashi, A.; Tatsumisago, M., Bulk-Type Lithium Metal Secondary Battery With Indium Thin Layer at Interface Between Li Electrode and Li_2S-P_2S_5 Solid Electrolyte. *Electrochemistry* **2012,** *80* (10), 734-736.
15. Kato, A.; Suyama, M.; Hotehama, C.; Kowada, H.; Sakuda, A.; Hayashi, A.; Tatsumisago, M., High-Temperature Performance of All-Solid-State Lithium-Metal Batteries Having Li/Li_3PS_4 Interfaces Modified With Au Thin Films. *J. Electrochem. Soc.* **2018,** *165* (9), A1950.

16. Zheng, C.; Zhang, J.; Xia, Y.; Huang, H.; Gan, Y.; Liang, C.; He, X.; Tao, X.; Zhang, W., Unprecedented Self-Healing Effect of Li6PS5Cl-Based All-Solid-State Lithium Battery. *Small* **2021,** *17* (37), 2101326.
17. Yubuchi, S.; Teragawa, S.; Aso, K.; Tadanaga, K.; Hayashi, A.; Tatsumisago, M., Preparation of High Lithium-Ion Conducting Li_6PS_5Cl Solid Electrolyte From Ethanol Solution for All-Solid-State Lithium Batteries. *J. Power Sources* **2015,** *293*, 941-945.
18. Liu, S.; Zhou, L.; Han, J.; Wen, K.; Guan, S.; Xue, C.; Zhang, Z.; Xu, B.; Lin, Y.; Shen, Y., Super Long-Cycling All-Solid-State Battery with Thin Li_6PS_5Cl-Based Electrolyte. *Adv. Energy Mater.* **2022,** *12* (25), 2200660.
19. Zhang, J.; Zheng, C.; Li, L.; Xia, Y.; Huang, H.; Gan, Y.; Liang, C.; He, X.; Tao, X.; Zhang, W., Unraveling the Intra and Intercycle Interfacial Evolution of Li_6PS_5Cl-Based All-Solid-State Lithium Batteries. *Adv. Energy Mater.* **2020,** *10* (4), 1903311.
20. Santhosha, A.; Medenbach, L.; Buchheim, J. R.; Adelhelm, P., The Indium–Lithium Electrode in Solid-State Lithium-Ion Batteries: Phase Formation, Redox Potentials, and Interface Stability. *Batter. Supercaps* **2019,** *2* (6), 524-529.
21. Rao, R. P.; Sharma, N.; Peterson, V.; Adams, S., Formation and Conductivity Studies of Lithium Argyrodite Solid Electrolytes Using In-Situ Neutron Diffraction. *Solid State Ion.* **2013,** *230*, 72-76.
22. Yu, C.; van Eijck, L.; Ganapathy, S.; Wagemaker, M., Synthesis, Structure and Electrochemical Performance of the Argyrodite Li_6PS_5Cl Solid Electrolyte for Li-Ion Solid State Batteries. *Electrochim. Acta* **2016,** *215*, 93-99.
23. Doerrer, C.; Capone, I.; Narayanan, S.; Liu, J.; Grovenor, C. R.; Pasta, M.; Grant, P. S., High Energy Density Single-Crystal NMC/Li_6PS_5Cl Cathodes for All-Solid-State Lithium-Metal Batteries. *ACS Appl. Mater. Interfaces* **2021,** *13* (31), 37809-37815.
24. Randrema, X.; Barcha, C.; Chakir, M.; Viallet, V.; Morcrette, M., A Detailed Characterisation Study of Li_6PS_5Cl Ionic Conductors From Several Synthetic Routes. *Solid State Sci.* **2021,** *118*, 106681.
25. Yu, C.; Ganapathy, S.; Hageman, J.; Van Eijck, L.; Van Eck, E. R.; Zhang, L.; Schwietert, T.; Basak, S.; Kelder, E. M.; Wagemaker, M., Facile Synthesis Toward the Optimal Structure-Conductivity Characteristics of the Argyrodite Li_6PS_5Cl Solid-State Electrolyte. *ACS Appl. Mater. Interfaces* **2018,** *10* (39), 33296-33306.
26. Wang, S.; Zhang, Y.; Zhang, X.; Liu, T.; Lin, Y.-H.; Shen, Y.; Li, L.; Nan, C.-W., High-Conductivity Argyrodite Li_6PS_5Cl Solid Electrolytes Prepared via Optimized Sintering Processes for All-Solid-State Lithium–Sulfur Batteries. *ACS Appl. Mater. Interfaces* **2018,** *10* (49), 42279-42285.
27. Narayanan, S.; Ulissi, U.; Gibson, J. S.; Chart, Y. A.; Weatherup, R. S.; Pasta, M., Effect of Current Density on the Solid Electrolyte Interphase Formation at the Lithium|Li_6PS_5Cl Interface. *Nat. Commun.* **2022,** *13* (1), 7237.
28. Wang, C.; Deng, T.; Fan, X.; Zheng, M.; Yu, R.; Lu, Q.; Duan, H.; Huang, H.; Wang, C.; Sun, X., Identifying Soft Breakdown in All-Solid-State Lithium Battery. *Joule* **2022,** *6* (8), 1770-1781.
29. Counihan, M. J.; Chavan, K. S.; Barai, P.; Powers, D. J.; Zhang, Y.; Srinivasan, V.; Tepavcevic, S., The Phantom Menace of Dynamic Soft-Shorts in Solid-State Battery Research. *Joule* **2024,** *8* (1), 64-90.

30. Shi, X.; Zeng, Z.; Sun, M.; Huang, B.; Zhang, H.; Luo, W.; Huang, Y.; Du, Y.; Yan, C., Fast Li-Ion Conductor of Li_3HoBr_6 for Stable All-Solid-State Lithium–Sulfur Battery. *Nano Lett.* **2021,** *21* (21), 9325-9331.
31. Liang, J.; Li, X.; Wang, S.; Adair, K. R.; Li, W.; Zhao, Y.; Wang, C.; Hu, Y.; Zhang, L.; Zhao, S., Site-Occupation-Tuned Superionic Li_xScCl_{3+x} Halide Solid Electrolytes for All-Solid-State Batteries. *J. Amer. Chem. Soc.* **2020,** *142* (15), 7012-7022.
32. Wood, K. N.; Noked, M.; Dasgupta, N. P., Lithium Metal Anodes: Toward an Improved Understanding of Coupled Morphological, Electrochemical, and Mechanical Behavior. *ACS Energy Lett.* **2017,** *2* (3), 664-672.
33. Lin, D.; Zhao, J.; Sun, J.; Yao, H.; Liu, Y.; Yan, K.; Cui, Y., Three-Dimensional Stable Lithium Metal Anode With Nanoscale Lithium Islands Embedded in Ionically Conductive Solid Matrix. *PANS* **2017,** *114* (18), 4613-4618.
34. Schlenker, R.; Stępień, D.; Koch, P.; Hupfer, T.; Indris, S.; Roling, B.; Miß, V.; Fuchs, A.; Wilhelmi, M.; Ehrenberg, H., Understanding the Lifetime of Battery Cells Based on Solid-State Li_6PS_5Cl Electrolyte Paired With Lithium Metal Electrode. *ACS Appl. Mater. Interfaces* **2020,** *12* (17), 20012-20025.
35. Pang, B.; Gan, Y.; Xia, Y.; Huang, H.; He, X.; Zhang, W., Regulation of the Interfaces Between Argyrodite Solid Electrolytes and Lithium Metal Anode. *Front. Chem* **2022,** *10,* 837978.
36. Yu, T.; Liang, J.; Luo, L.; Wang, L.; Zhao, F.; Xu, G.; Bai, X.; Yang, R.; Zhao, S.; Wang, J., Superionic Fluorinated Halide Solid Electrolytes for Highly Stable Li-Metal in All-Solid-State Li Batteries. *Adv. Energy Mater.* **2021,** *11* (36), 2101915.
37. Xin, F.; Zhou, H.; Chen, X.; Zuba, M.; Chernova, N.; Zhou, G.; Whittingham, M. S., Li–Nb–O Coating/Substitution Enhances the Electrochemical Performance of the $LiNi_{0.8}Mn_{0.1}Co_{0.1}O_2$ (NMC 811) Cathode. *ACS Appl. Mater. Interfaces* **2019,** *11* (38), 34889-34894.
38. Peng, L.; Ren, H.; Zhang, J.; Chen, S.; Yu, C.; Miao, X.; Zhang, Z.; He, Z.; Yu, M.; Zhang, L., $LiNbO_3$-Coated $LiNi_{0.7}Co_{0.1}Mn_{0.2}O_2$ and Chlorine-Rich Argyrodite Enabling High-Performance Solid-State Batteries Under Different Temperatures. *Energy Storage Mater.* **2021,** *43*, 53-61.
39. Li, X.; Jin, L.; Song, D.; Zhang, H.; Shi, X.; Wang, Z.; Zhang, L.; Zhu, L., $LiNbO_3$-coated $LiNi_{0.8}Co_{0.1}Mn_{0.1}O_2$ Cathode With High Discharge Capacity and Rate Performance for All-Solid-State Lithium Battery. *J. Energy Chem.* **2020,** *40*, 39-45.
40. Kim, Y.-J.; Rajagopal, R.; Kang, S.; Ryu, K.-S., Novel Dry Deposition of $LiNbO_3$ or Li_2ZrO_3 on $LiNi_{0.6}Co_{0.2}Mn_{0.2}O_2$ for High Performance All-Solid-State Lithium Batteries. *Chem. Eng. J.* **2020,** *386*, 123975.
41. Liu, L.; Chen, L.; Huang, X.; Yang, X.-Q.; Yoon, W.-S.; Lee, H.; McBreen, J., Electrochemical and In Situ Synchrotron XRD Studies on Al_2O_3-Coated $LiCoO_2$ Cathode Material. *J. Electrochem. Soc.* **2004,** *151* (9), A1344.
42. Reimers, J.; Dahn, J.; Von Sacken, U., Effects of Impurities on the Electrochemical Properties of $LiCoO_2$. *J. Electrochem. Soc.* **1993,** *140* (10), 2752.
43. Li, Q.; Qiao, R.; Wray, L. A.; Chen, J.; Zhuo, Z.; Chen, Y.; Yan, S.; Pan, F.; Hussain, Z.; Yang, W., Quantitative Probe of the Transition Metal Redox in Battery Electrodes Through Soft X-Ray Absorption Spectroscopy. *J. Phys. D: Appl. Phys.* **2016,** *49* (41), 413003.

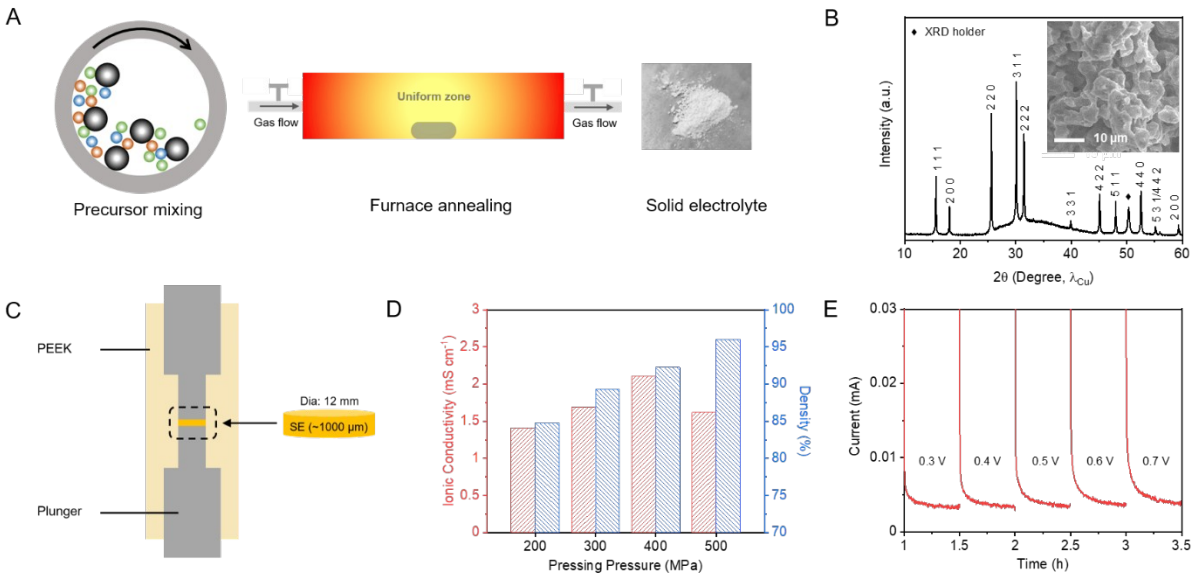

Figure 1. Synthesis and physical characterization of Li_6PS_5Cl argyrodite electrolyte. (A) Schematic of the argyrodite synthesis process; (B) XRD pattern with inset SEM image, Bragg reflections of Li_6PS_5Cl are indexed as (hkl); (C) schematic of the setup for conductivity measurements; (D) ionic conductivity and density at varied pressures; and (E) DC polarization for electrical conductivity.

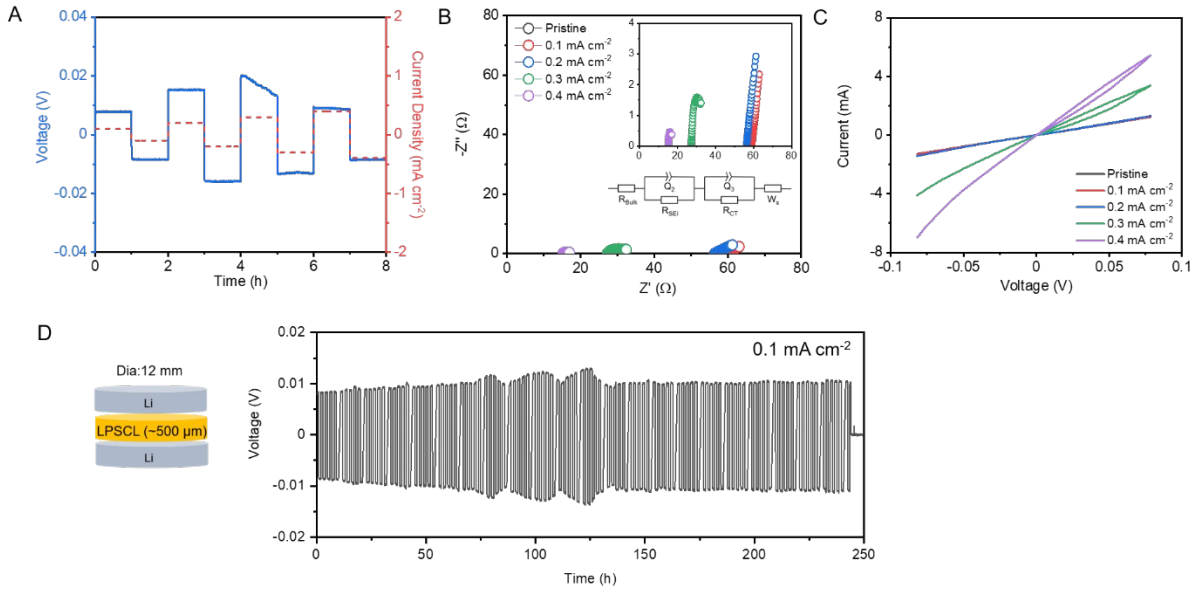

Figure 2. Electrochemical characterization of Li|Li_6PS_5Cl|Li symmetric cell. (A) CCD test, (B) EIS spectra with inset equivalent circuit and enlarged spectra, (C) CV curves, and (D) charge-discharge profiles cycled at 0.1 mA cm^{-2}.

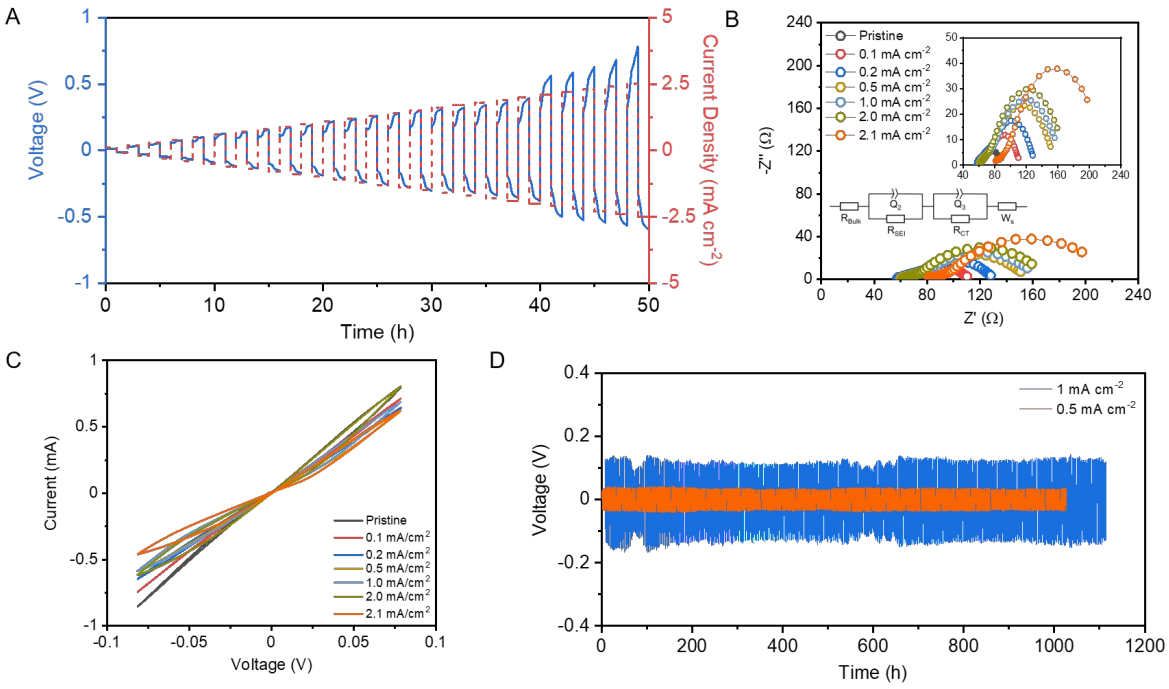

Figure 3. Electrochemical characterization of $Li_{0.5}In|Li_6PS_5Cl|Li_{0.5}In$ symmetric cell. (A) CCD test, (B) EIS spectra with inset equivalent circuit and enlarged spectra, (C) CV curves, and (D) charge-discharge profiles cycled at 0.5 and 1 mA cm^{-2}.

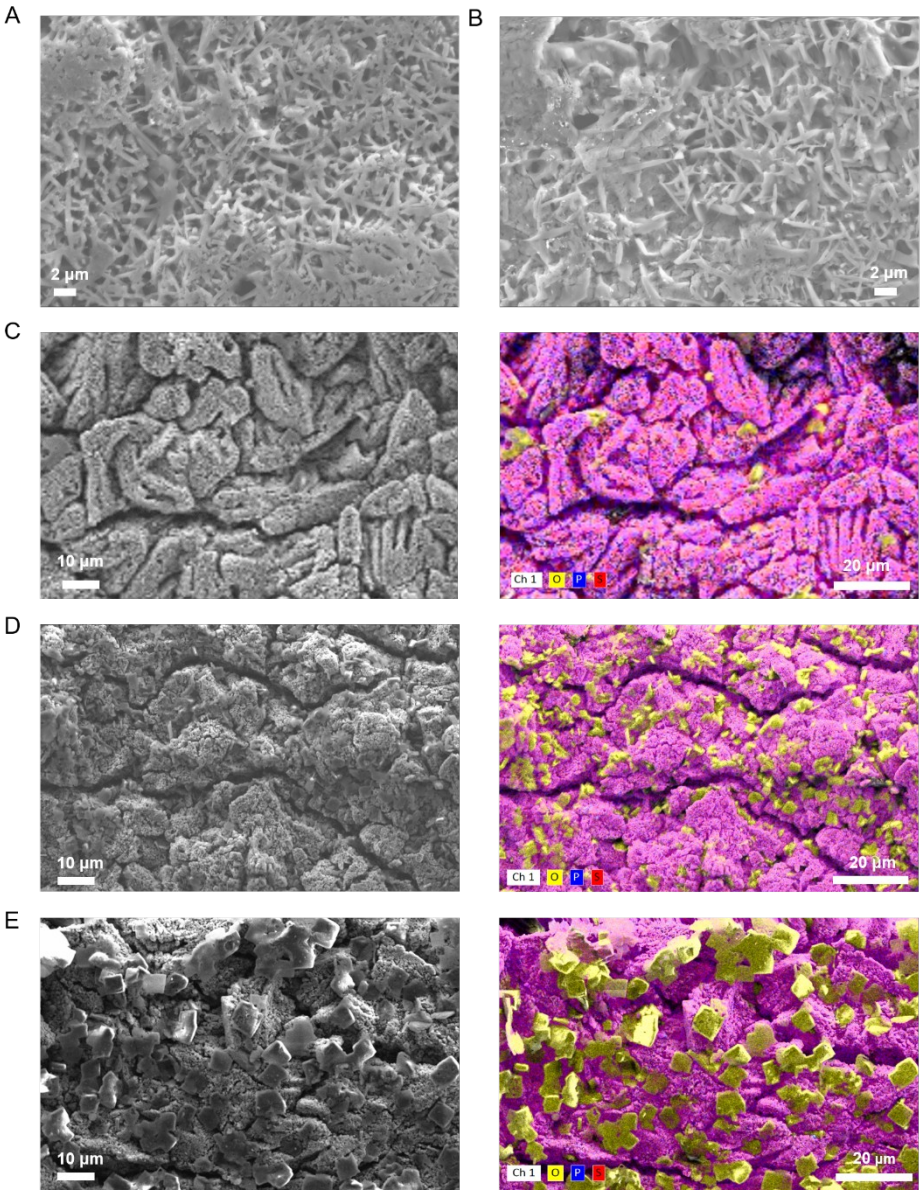

Figure 4. SEM images and EDS maps collected on Li_6PS_5Cl electrolyte after long-term cycling in symmetric cells with various anodes. Top-view SEM of Li_6PS_5Cl interface with (A) $Li_{0.5}In$ and (B) LiIn anode, and cross-section SEM and EDS of Li_6PS_5Cl with (C) $Li_{0.5}In$, (D) LiIn, and (E) pure Li anode. The pink map shows the combined sulfur (red) and phosphorus (blue), representing the distribution of solid electrolyte, while the yellow map is oxygen originating from lithium oxide that forms due to the oxidation of Li during sample transfer. The $Li_{0.5}In$ and LiIn samples were collected after cycling at 0.5 mA cm^{-2} for 1000 h and the Li sample was collected after a short circuit.

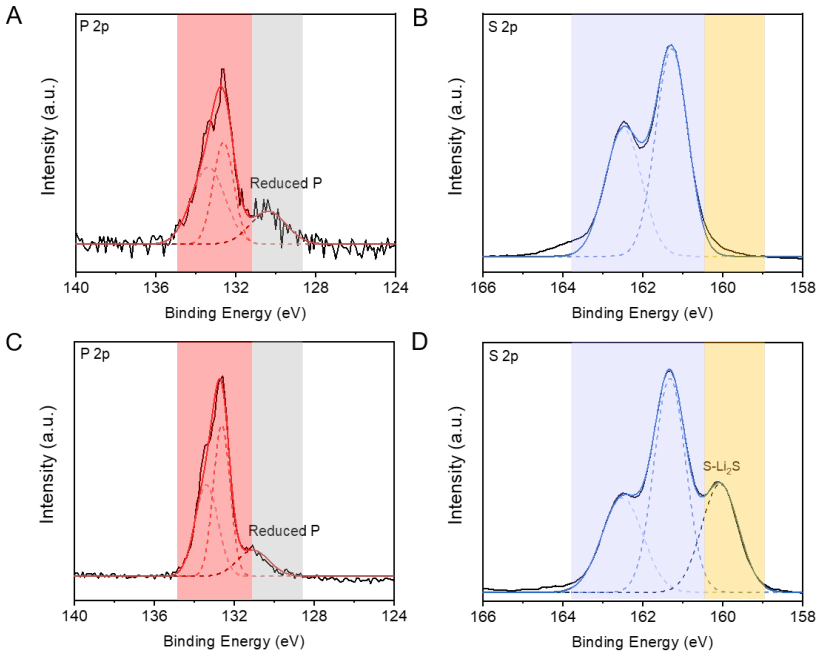

Figure 5. XPS spectra of P 2p and S 2p on Li_6PS_5Cl interfaces with (A, B) $Li_{0.5}In$ and (C, D) LiIn anode.

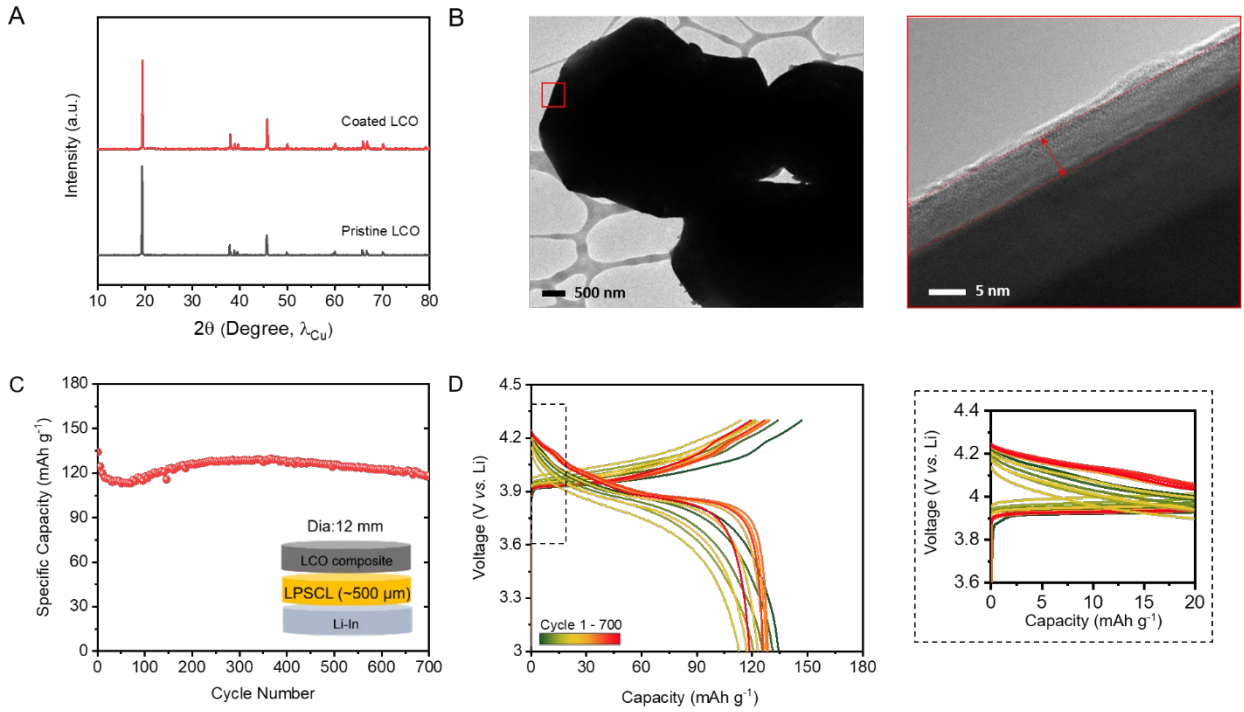

Figure 6. Electrochemical performance of $LiCoO_2|Li_6PS_5Cl|Li_{0.5}In$ full cell. (A) XRD patterns and (b) TEM images of $LiCoO_2$ and $LiNbO_3$-coated $LiCoO_2$, (C) cycling performance with inset of all solid-state full cell configuration, (D) voltage profiles during cycling. The cells are cycled between 4.3 and 3 V vs. (Li^+/Li) at 14 mA g^{-1}.

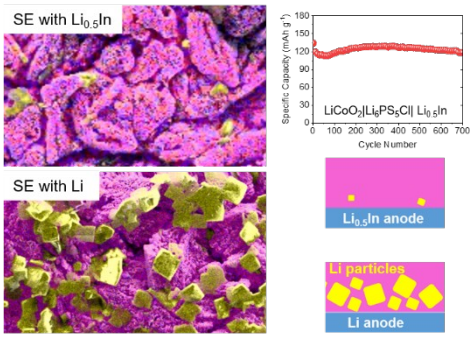

For Table of Contents Use Only

Supporting Information for

Unveiling the Role of Lithium Iodide in Stabilizing Solid Interfaces in All-Solid-State Li Metal Batteries

Di Huang[1], Suyue Yuan[2], Nicole Adelstein[3], Gao Liu[1], Liwen F. Wan[2], and Wei Tong[1,*]

[1]Energy Storage and Distributed Resources Division, Lawrence Berkeley National Laboratory, Berkeley, California 94720, United States

[2]Laboratory for Energy Applications for the Future, Lawrence Livermore National Laboratory, Livermore, California 94550, United States

[3]Department of Chemistry and Biochemistry, San Francisco State University, San Francisco, CA 94132, United States

Email: weitong@lbl.gov

Experimental Methods

LPSCI powders were synthesized via a solid-state reaction. Raw materials, including Li_2S, LiCl, LiI, and P_2S_5, were sealed inside an Ar filled glovebox at specific molar ratios and ball-milled in a zirconium jar at 550 rpm for 24 h. The milled powder was then pressed into pelleted and annealed at 550 °C for 3 h in a tube furnace under Ar atmosphere. After annealing, the sample was grounded into powder and stored inside the Ar glovebox. Ionic and electrical conductivities were measured using electrochemical impedance spectroscopy (EIS) and direct current (DC) method, respectively. Ionic conductivity was calculated using the equation: $\sigma = I/RA$, where I is the pellet thickness, R is the bulk resistance measured by EIS, and A is the pellet area. Electrical conductivity was measured using the same equation, and R is indicated by the slope between the voltage and the current. X-ray diffraction (XRD) patterns were collected in an airtight holder on the Bruker D2-Phaser with Cu Kα radiation (λ = 1.54178 Å) from 10 to 55°.

An *in situ* asymmetric solid-state cell was assembled using a configuration described in our previous report.[1] The indium tin oxide (ITO) glass allows for visualization of Li plating/stripping behaviors. The electrochemical characterization was conducted at room temperature using biologic workstation. Galvanostatic charge/discharge were carried out at different current densities and the Li plating/stripping processes were monitored using a Nikon LV100 digital microscope with the Lumenera INFINITY 3 camera and 10x/20x objective lens. After cycling, the cells were disassembled to harvest the SE pellet and ITO current collector for the interface characterization. Scanning electron microscopy (SEM) images and energy dispersive X-ray spectroscopy (EDS) maps were obtained on the Zeiss Gemini Ultra-55 Analytical Field Emission Scanning Electron Microscope coupled to a Bruker X-Ray Energy Dispersive Spectrometer at the voltage of 10 kV.

DFT calculations were performed using the Vienna Ab Initio Simulation Package (VASP) with the Perdew, Burke, and Ernzerhof (PBE) type generalized gradient approximation (GGA) approximation.[2] The projector augmented wave (PAW) pseudopotentials were used to represent ion electron interactions for all elements[3] and to account for dispersion interactions, the DFT-D3 method with a Becke-Johnson damping function was employed.[4] A plane-wave basis set with a cutoff energy of 600 eV was utilized, with proper k-point sampling to ensure numerical convergence. For all structural relaxations, the energy and forces were converged to 10^{-6} eV and 0.01 eV/Å, respectively. For the calculations of Li-ion diffusion, the climbing-image nudged elastic band method[5] was used with a background charge of -1 implemented in a 215-atom supercell to model Li^+ migration to the nearest vacancy site. The activation energies were obtained when the residual forces on each moving image along Li-ion migration path are smaller than 0.05 eV/Å.

Movie S1. *In situ* optical microscopy observation, showing the Li plating behavior during the 1st cycle at 10 μA cm^{-2}. The movie clip is accelerated by 100 times.

Movie S2. *In situ* optical microscopy observation, showing the Li stripping behavior during the 1st cycle at 10 μA cm^{-2}. The movie clip is accelerated by 100 times.

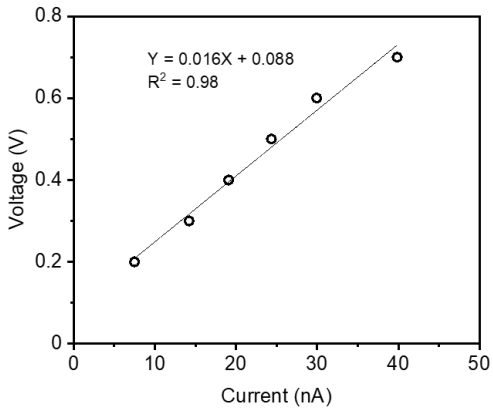

Figure S1. Electrical conductivity of LPSCI-30 electrolyte, indicated by the slope between the voltage and current measured from DC polarization.

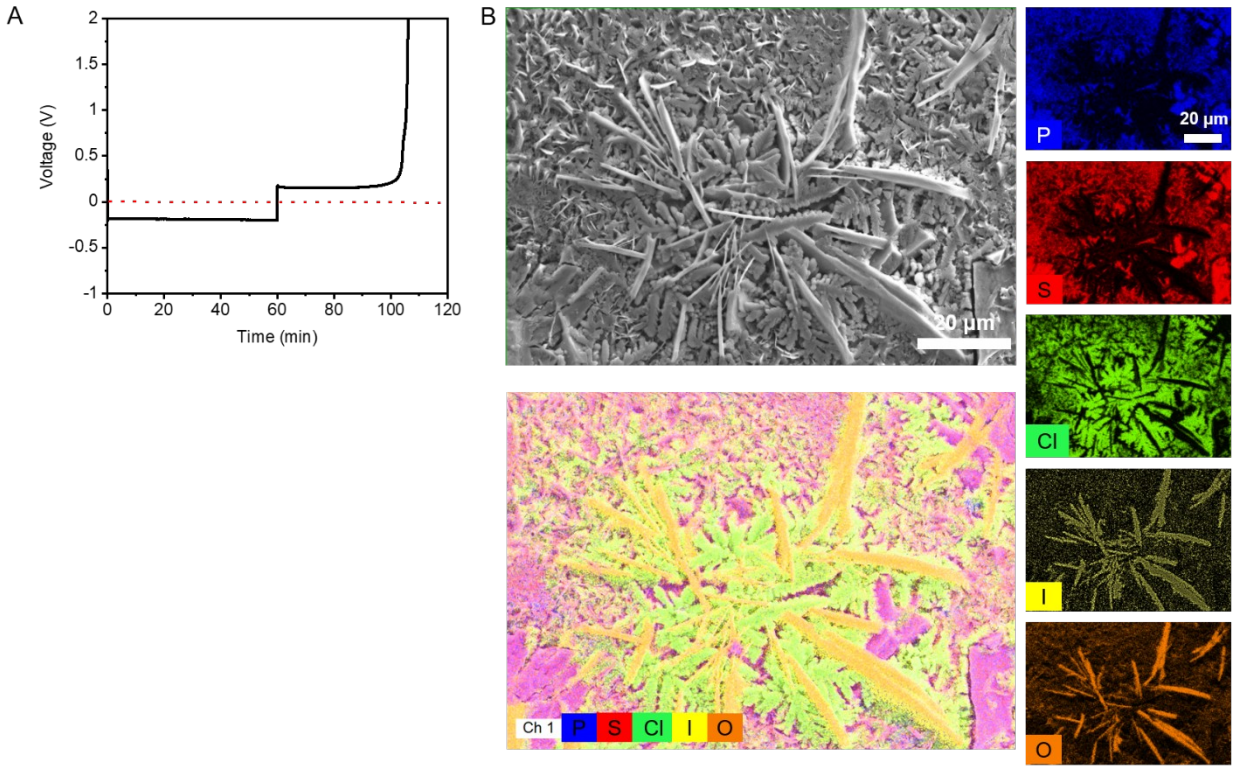

Figure S2. (A) Voltage profiles of the asymmetric cell cycled with LPSCI-30 electrolyte at 100 mA cm^{-2}. (B) SEM image and EDS maps collected on the LPSCI-30 electrolyte after the 1st stripping.

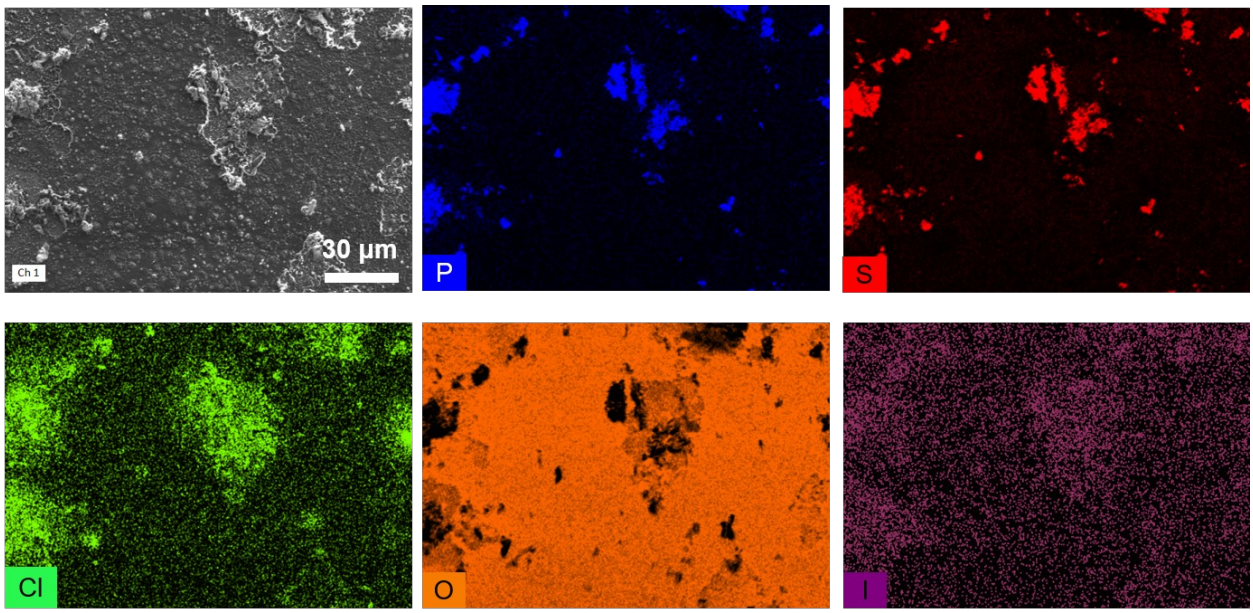

Figure S3. SEM image and EDS maps collected on the ITO after the 1st stripping with LPSCI-30 electrolyte.

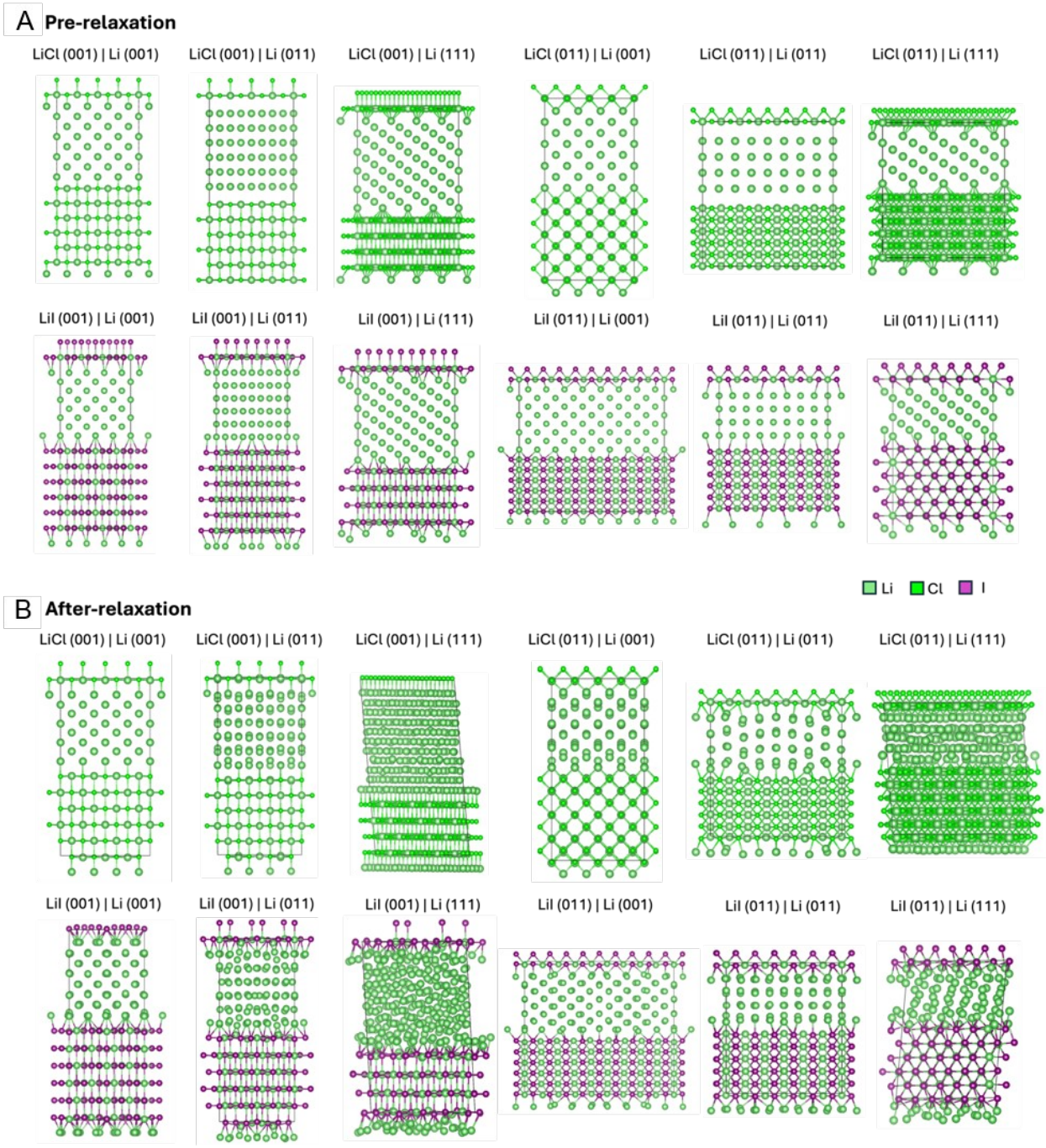

Figure S4. Structure representation of Li-halide | Li metal interface models. (A) Pre-relaxed and (B) post-relaxed atomic configurations of each interface model.

Table S1. Ionic and electronic conductivities of the as-prepared LPSCI argyrodites with 10%, 30%, 50% iodide substitution, denoted as LPSCI-10, LPSCI-30, and LPSCI-50, respectively.

Sample	**Ionic Conductivity (S cm^{-1})**	**Electrical Conductivity (S cm^{-1})**
LPSCI	2.8×10^{-3}	4.3×10^{-9}
LPSCI-10	2.6×10^{-3}	2.3×10^{-9}
LPSCI-30	0.9×10^{-3}	6.4×10^{-9}
LPSCI-50	0.3×10^{-3}	10.1×10^{-9}

Table S2. Calculated interfacial energies of Li-halide (LiX) | Li metal interfaces.

Interface Model	LiCl (J m^{-2})	LiI (J m^{-2})
LiX (001) | Li (001)	0.4984	0.4621
LiX (001) | Li (011)	0.6293	0.5478
LiX (001) | Li (111)	0.4407	0.4878
LiX (011) | Li (001)	0.6972	0.6108
LiX (011) | Li (011)	0.6306	0.4860
LiX (011) | Li (111)	0.6106	0.3948

Table S3. Model parameters of Li-halide | Li metal interfaces.

Slab A	Slab B	a (Å)	b (Å)	$\bar{\varepsilon}$ (%)	γ (°)	# of atoms	k-point mesh (a, b, c)
LiCl (001)	Li (001)	14.144	14.144	1.17	90	320	$3\times3\times2$
LiI (001)	Li (001)	13.629	13.629	2.31	90	248	$3\times3\times1$
LiCl (001)	Li (011)	20.308	10.147	1.14	45	336	$2\times3\times1$
LiI (001)	Li (011)	13.998	18.695	2.06	82	360	$3\times2\times1$
LiCl (001)	Li (111)	35.013	8.878	3.58	154	392	$1\times6\times2$
LiI (001)	Li (111)	20.582	15.972	2.34	128	344	$2\times3\times2$
LiCl (011)	Li (001)	14.582	14.146	4.02	90	320	$3\times3\times2$
LiI (011)	Li (001)	32.676	12.836	2.99	65	472	$1\times3\times2$
LiCl (011)	Li (011)	13.135	20.224	3.15	79	296	$3\times2\times2$
LiI (011)	Li (011)	14.251	20.153	2.81	90	272	$3\times2\times2$
LiCl (011)	Li (111)	20.590	17.844	3.04	63	392	$2\times3\times2$
LiI (011)	Li (111)	34.179	9.336	2.25	155	272	$1\times4\times2$

REFERENCES

1. Huang, D.; Liu, G.; Tong, W., In Situ Characterization of Interface Evolution in Argyrodite-Based All-Solid-State Li Batteries. *Small* **2024**, 2406862.
2. Perdew, J. P.; Ernzerhof, M.; Burke, K., Rationale for Mixing Exact Exchange with Density Functional Approximations. *J. Chem. Phys.* **1996,** *105*, 9982-9985.
3. Blöchl, P. E., Projector Augmented-Wave Method. *Phys. Rev. B* **1994,** *50*, 17953-17979.
4. Grimme, S.; Ehrlich, S.; Goerigk, L., Effect of the Damping Function in Dispersion Corrected Density Functional Theory. *J. Comput. Chem.* **2011,** *32*, 1456-1465.
5. Henkelman, G.; Uberuaga, B. P.; Jónsson, H., A Climbing Image Nudged Elastic Band Method for Finding Saddle Points and Minimum Energy Paths. *J. Chem. Phys.* **2000,** *113*, 9901-9904.